Theor Chem Acc (2011) 130:1071–1082
DOI 10.1007/s00214-011-0993-x

REGULAR ARTICLE

Proposed model for growth preference of plate-like nanohydroxyapatite crystals on superhydrophilic vertically aligned carbon nanotubes by electrodeposition

A. O. Lobo · F. R. Marciano · I. Regiani · S. C. Ramos · J. T. Matsushima · E. J. Corat

Received: 4 April 2011 / Accepted: 5 July 2011 / Published online: 30 July 2011

Abstract For the first time, the mechanism of growth of plate-like n-HA electrodeposited on superhydrophilic vertically aligned multi-walled carbon nanotubes (VACNT) is presented and a model for the specific growth preference is discussed. Results show that the carboxyl (carboxylic acid)/carboxylate functional groups directly attached on VACNT tips after oxygen plasma treatment were essential for the acceleration of the OH^- formation and the deposition of plate-like HA crystals. FEG-SEM, EDX and XRD showed that a homogeneous highly crystalline HA film, stoichiometric and with preferential growth in the (002) plane direction, was formed.

Dedicated to Professor Akira Imamura on the occasion of his 77th birthday and published as part of the Imamura Festschrift Issue.

A. O. Lobo (✉) · F. R. Marciano
Laboratorio de Nanotecnologia Biomedica (NanoBio), Universidade do Vale do Paraíba (UniVaP), Avenida Shishima Hifumi 2911, Urbanova, São José dos Campos, SP 12244-000, Brazil
e-mail: loboao@yahoo.com

A. O. Lobo · F. R. Marciano
Laboratorio de Espectroscopia Vibracional Biomedica (LEVB), Instituto de Pesquisa e Desenvolvimento, Universidade do Vale do Paraiba, Avenida Shishima Hifumi 2911, Urbanova, São José dos Campos, SP 12244-000, Brazil

I. Regiani
Instituto Tecnológico de Aeronáutica (ITA), Praça Marechal Eduardo Gomes 50, Vila das Acácias, São José dos Campos, SP 12228-900, Brazil

S. C. Ramos · J. T. Matsushima · E. J. Corat
Laboratorio Associado de Sensores e Materiais (LAS), Instituto Nacional de Pesquisas Espaciais (INPE), Avenida dos Astronautas 1758, Jardin da Granja, São José dos Campos, SP 12227-010, Brazil

Keywords Carbon nanotubes · Vertically aligned · Superhydrophilic · Hydroxyapatite · Electrodeposition · Plasma etching · Plate-like crystals

1 Introduction

Hydroxyapatite (HA, $Ca_{10}(PO_4)_6(OH)_2$) is a form of calcium phosphate that bears close chemical likeness with the mineral part of bones and teeth tissues [1]. It promotes tissue attachment and bone growth by spontaneously forming a biologically active bone-like apatite layer over its surface [2]. Thus, HA is classified as a biocompatible and bioactive material, and crystalline HA has been found in many biological applications such as dental or skeletal implants and bone repair scaffolds [3]. There has been a resurgent interest in controlling HA crystal nucleation, crystallinity and growth for assembling composite materials, analogous to those produced by nature, involving the biomineralization process [4]. It was recognized that poor crystallinity can directly affect the natural precipitation of apatite that promotes natural osteointegration [5]. Traditional clinical applications of calcium phosphates have mainly focused on highly crystalline ceramics [5]. For this reason, the development of crystalline nanobiomaterials is of particular interest in bone regenerative medicine.

Among other nanobiomaterials, vertically aligned multiwalled carbon nanotubes (VACNT) promise to play a great role in the study of tissue regeneration [6–10]. The electronic structure, surface morphology and exceptional mechanical properties of VACNT are typical of graphite-like structures [11, 12]. VACNT are fibrous because of their tubular construction with nanometric diameters and high aspect ratio [13, 14]. However, the potential biomedical application of this new nanobiomaterial class is

limited due to its hydrophobicity [15]. Several methods are used to control wettability of CNT, including forming oxygen-containing functional groups on the CNT surfaces by oxidative treatment [16] or acid treatment [17]. The wettability in polar liquids, such as water, improved significantly in this way, leading to more reactive VACNT surfaces [18]. Ramos et al. showed that oxygen plasma etching is the most efficient way to introduce polar groups (COH, OH, C=O, COOH) and roughness to VACNTs in order to obtain superhydrophilic behavior [19].

Some investigations have shown synthesis of HA on CNTs using various methods, such as crystal growth from simulated body fluid (SBF) [20], composite coatings deposition obtained by electrophoresis [21], aerosol application [22] or sol–gel matrix formation [23]. All these methods consisted of dispersing CNT in a HA solution. One showed that thermal treatment is necessary to obtain crystalline HA [21], while another showed that several weeks are required to obtain sufficient mineralization when the CNTs are soaked in SBF [20]. In addition, these authors clearly showed that the Ca- and P-rich layer consists of a carbonate-containing HA with a disordered structure and nonhomogeneous deposition and is thus poorly crystalline.

The electrodeposition is an advantageous method for producing a thin, crystalline, homogeneous and adherent film and is a rapid, reproducible, efficient and low cost process [24, 25]. The composition and control of the coating structure is possible in part because of the low processing temperature. The ability to coat irregular surfaces is also important. Therefore, the electrodeposition of HA coating has attracted noticeable attention in recent years. We have shown in a recent publication that superhydrophilic VACNT films efficiently grow platelet-like n-HA crystals directly on them [26].

In this paper, we propose a new n-HA electrodeposition mechanism using superhydrophilic VACNT films as a template. The general mechanism proposed for HA electrodeposition is explained using Ti as a substrate [24, 25]. The proposal of this work is to show a relationship between carboxyl (carboxylic acid)/carboxylate functional groups and preferential growth of n-HA crystals directly electrodeposited on superhydrophilic VACNT tips.

2 Materials and methods

2.1 Synthesis of carbon nanotubes

The VACNT films were produced as thin films using a microwave plasma chamber equipped with a 2.45-GHz microwave generator (MWCVD) [26–29]. The substrates were 10-mm titanium (Ti) squares covered by a thin Fe layer (10 nm) deposited by an e-beam evaporator. The Fe layers were pre-treated to promote nanocluster formation, which forms the catalyst for VACNT growth. The pre-treatment was carried out during 5 min in a plasma of N_2/H_2 (10/90sccm) with a substrate temperature of around 760 °C. After pre-treatment, CH_4 (14 sccm) was inserted in the chamber at a substrate temperature of 800 °C for 2 min. The reactor was kept at a pressure of 30 Torr during the whole process. More details about morphological and structural analyses are given elsewhere [26–29].

2.2 VACNT functionalized by polar groups

Functionalization of the nanotube tips by the incorporation of oxygen-containing groups was performed in a pulsed-direct current plasma reactor with an oxygen flow rate of 1 sccm, at a pressure of 80 mTorr, −700 V and with a frequency of 20 kHz [30]. The total time of the plasma etching was 120 s. The superhydrophilic properties are given elsewhere [31]. The incorporation of the polar groups was monitored by X-ray photoelectron spectroscopy (XPS), using an instrument from VG Microtech (XR 705) operating at 486.5 eV (AlKα).

2.3 Hydroxyapatite electrodeposition process on VACNTs films

The electrodeposition of the HA crystals on the VACNT films was performed using 0.042 mol L^{-1} $Ca(NO_3)_2 \cdot 4H_2O$ + 0.025 mol L^{-1} $(NH_4) \cdot 2HPO_4$ electrolytes (pH 4.7) [26]. The electrochemical measurements were carried out using a three-electrode cell coupled to an Autolab PGSTAT 302 instrument. Superhydrophilic VACNT films were used as the working electrode, and the geometric area in contact with electrolytic solution was 0.27 cm^2. A platinum coil wire served as the auxiliary electrode, and an Ag/AgCl electrode was used as the reference electrode. The HA films were produced by applying a constant potential of −2.0 V for 30 min while the solution temperature was maintained at 70 °C. Scanning of electron microscopy using a field emission gun (FEG-SEM, JEOL JSM-6330F) was used to observe the structure of HA crystal morphologies.

Semi-quantitative elemental analyses of calcium (Ca) and phosphorus (P) were carried out by a micro-X-ray fluorescence spectrometer by energy-dispersive (μ-EDX 1300, Shimadzu, Kyoto, Japan), equipped with a rhodium X-ray tube and a Si(Li) detector cooled by liquid nitrogen (N_2). The equipment was coupled to a computer system for data processing. The energy range of scans was from 0.0 to 40.0 eV. The voltage in the tube was set at 15 kV, with automatic current adjustment. The analyses of Ca and P characteristic emissions were taken longitudinally on the sample surfaces, with incident beam diameter of 50 μm.

The stepping mapping was taken using 40 × 30 points with a step of 20 μm along the n-HA on superhydrophilic VACNT films. Consequently, the analysis was performed in a line 100 μm long and 50 μm thick. The scans were performed with a count rate of 10 s per point (live time) and a dead time of 25%. The equipment was adjusted using a certified commercial reagent of stoichiometric hydroxyapatite (Aldrich, synthetic $Ca_{10}(PO_4)_6(OH)_2$, grade 99.999%, lot 10818HA) as reference. The measurements were collected using the fundamental parameters of characteristic X-ray emission of the elements Ca and P. The elements O and H were used as chemical balance. The reference was also used as a point in the intensity curve calibration. The energy calibration was performed using internal standards for light elements.

Surface chemical compositions of the n-HA were investigated by Fourier transform infrared attenuated total reflection spectroscopy (FT-IR ATR: Spectrum Spotlight-400, Perkin Elmer) and Raman spectroscopy (Renishaw micro-Raman model 2000 with an Ar ion laser, $\lambda = 514.5$ nm).

The structural analysis of HA crystals was performed by X-ray diffractometry (X-Pert Philips) with Cu K-α radiation generated at 40 kV and 50 mA. Crystal size of the HA phase (thkl) was calculated using Scherer's formula. The HA plane's preferential growth was calculated using the equation suggested by Hu et al. [32] All the results were compared to standard powder HA sample (JCPDS 9-432).

3 Results and discussions

Figure 1 shows the morphological and structural VACNT analyses before and after exposure to the oxygen plasma. Figure 1a shows a SEM image of the high density of the as-grown VACNT film grown on Fe catalyst. VACNTs presented a length of 6–8 μm. Figure 1b shows a TEM image of typical internal bamboo-like structures of the VACNT. Figure 1c shows a SEM image after the oxygen plasma etching, and Fig. 1d shows structural changes. Visually, no significant morphological or structural changes could be observed on converting superhydrophilic VACNT films. No contaminants from either metallic particles or amorphous carbon were observed outside the tubes. Virtually, all metallic particles are enclosed by the VACNT produced, because the MWCVD uses all catalyst nanoclusters. The high atomic hydrogen concentration in the gas mixture efficiently removes residues from the amorphous carbon.

Figure 2 shows the efficiency of the oxygen plasma treatment on converting VACNT surfaces from superhydrophobic to superhydrophilic behavior. The comparison of as-grown VACNT before and after the plasma treatment was studied using CA (a-b) and XPS (c-f) techniques. Systematic studies using polar and dispersive components using different liquids are shown in other publications [19, 31]. From the pulsed-direct current oxygen plasma treatment used in this work, a significant change on the contact angle from ∼154° (Fig. 2a) to ∼0° (Fig. 2b) was achieved. Hence, the VACNT surface switched from superhydrophobic to superhydrophilic, showing the high efficiency of this treatment.

To assess specific carboxyl (carboxylic acid)/carboxylate groups attached on surface, the C1s and O1s spectra were deconvoluted (Fig. 2c–f). A deconvolution comparison between as-grown VACNT (Fig. 2c, e) and after plasma functionalization (Fig. 2d, f) is shown. All binding energies were referenced to C1s at 284.1 eV. The spectra were deconvoluted by assuming a Lorentzian–Gaussian sum of functions (20% Lorentzian maximum contribution) [31]. The spectra were analyzed using Spectrum software XPS peak41 [33]. The C1s band was decomposed into five Gaussian components, referring to the bonds: C=C (∼284.1 eV), C–O (∼286.2 eV), C=O (286.8 eV), $–COO^-$ (288.1 eV) and the last one at 290.1 eV assigned to the shake-up peak (π–π* transitions) [34–37].

The intensity of the C=O peak especially the $–COO^-$ peak increased after the plasma etching. From these fits, the *widths at half maxima* (*FWHM*) showed an increase and suitable shifts for all bands after oxygen plasma treatment (data shown in Fig. 2d and Table 1). This implies strong C and O bond formation [34–37], mainly carboxyl (carboxylic acid)/carboxylate groups situated at the ends of the tubes. Datsyuka et al. [34] also showed that a suitable shift occurs for all bands attributed to carboxyl (carboxylic acid)/carboxylate groups after oxidation using HCl solution. Table 1 shows all the data collected and calculated from deconvolution of the C1s XPS peaks.

Figure 2e and f show deconvolution of the O1s spectra. In the literature, the oxygen peak for carbon materials is frequently decomposed into two components: one in the range 531.2–532.6 eV, attributed to oxygen doubly bound to carbon, and the second in the range 532.8–533.1 eV, attributed to oxygen singly bound to carbon [37]. Figure 2e and f show four peaks. To assume two different oxygen species is further supported in our case by the large full widths at half maxima (FWHM) for the experimental O1s peaks. For as-grown VACNT (Fig. 2e), these four components are found at 531.2 (C=O), 532.5 (C–OH), 533.4 (COOH–) and 534.5 eV (C–O) assigned as carboxylate [37, 38], oxygen doubly bonded to carbon in carboxylic acids and esters [37–39] and possibly –C–O (534.5 eV) or absorbed H_2O [40]. Table 2 shows all the data collected and calculated from deconvolution of the O1s XPS peaks. Exposure to the oxygen plasma (Fig. 2f) promoted a progressive increase in all oxygen groups, mainly in the

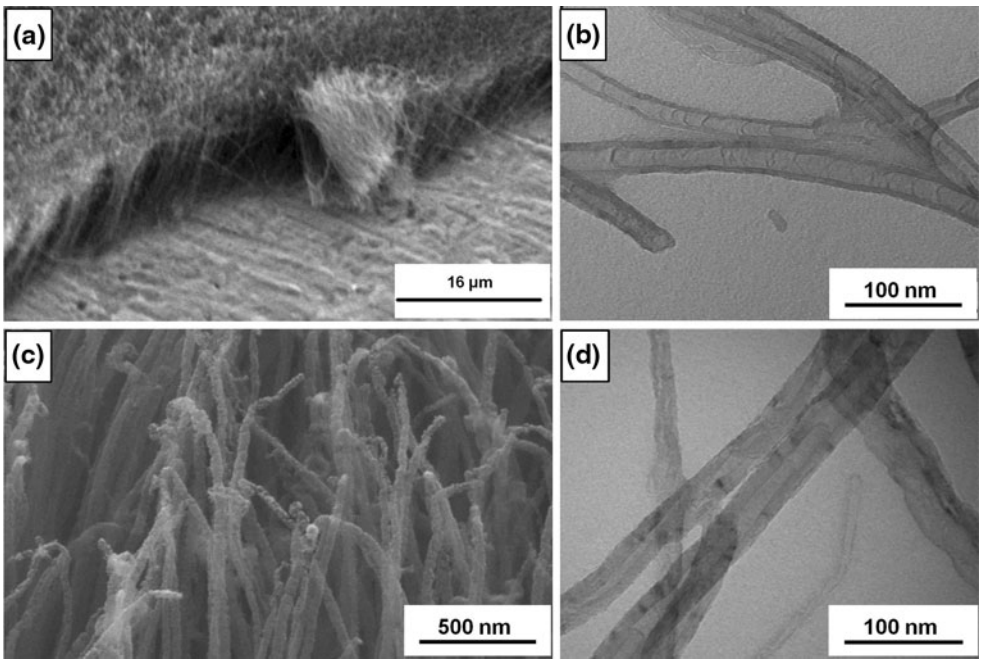

Fig. 1 SEM images of the as-grown **a** and **c** superhydrophilic VACNT films obtained by Fe catalysis. TEM images of bamboo-like structure of **b** as-grown and **d** superhydrophilic VACNT after the oxygen plasma etching

FWHMs, which increased (data shown in Table 2). In the quantitative analysis, an increase from 2.8% (Fig. 2e) to 18.9% after the oxygen plasma treatment (Fig. 2f) was observed in the oxygen content.

The use of oxygen plasma treatment on VACNT surfaces has already been reported in the literature [18, 41]. However, all reported works showed only a partial change on the wettability of the CNT surface due to the low concentration of carboxyl (carboxylic acid)/carboxylate groups attached to CNT tips (values up to 14%) [41]. Chirila et al. demonstrated that the wettability increased up to 68% after the treatment with microwave plasma and 20% with radio frequency plasma as compared to the untreated CNT [42]. Brandl and Marginean showed that the contact angle with water decreased from 88° to 58° after plasma treatment [43]. The plasma conditions (oxygen flow rate of 1 sccm, at a pressure of 80 mTorr, −700 V and total time 120 s) used in the present work show a higher efficiency compared with the previous reports due to higher concentration of carboxyl (carboxylic acid) groups directly attached to the VACNT tips.

The superhydrophilicity of the VACNT films obtained after the oxygen plasma treatment was a requirement for obtaining n-HA/VACNT composites by the electrodeposition method. As previously described, this is a new method to obtain n-HA/VACNT nanocomposites that achieves excellent bioactivity and cytocompatibility characteristics.

Figure 3 shows SEM images of plate-like n-HA grown directly on superhydrophilic VACNT tips after 30 min of electrodeposition. More details about the electrodeposition process were given elsewhere [26]. Notice that thin HA crystal films (with thicknesses of 3.5 μm) were grown without affecting the alignment of superhydrophilic VACNT films (Fig. 3a). Figure 3b shows the SEM of surface morphology and structures of the as-deposited HA coating. The coated surface exhibited different crystal characteristics and orientations. Details of the length (1–3 μm), thickness (1–3 nm) and orientation of crystals shape are shown in Fig. 3c. The high level of porosity observed in all the structures may be related to the formation of bubbles during the electrodeposition process and the 3D structures formed by superhydrophilic VACNTs films.

The elemental composition of the coating was investigated by energy-dispersive X-ray (EDX) mapping analysis of the n-HA crystals grown on the VACNTs (Fig. 4). The Ca and P content profiles (% wt) as a function of depth (μm) for each group are shown. The Ca/P ratio determined from the analysis was ∼1.64 (data media of three points, area: 0.8 × 0.6 mm), a value near that of the stoichiometric HA (1.67) present in bone tissue [44].

Raman and infrared spectroscopies are powerful physicochemical vibrational spectroscopic techniques that can be used for HA structural analysis. Typical calcium phosphates grown on superhydrophilic VACNTs films after electrodeposition process are shown in Fig. 5. The sharp band at 961 cm^{-1} is characteristic of crystalline n-HA. For the n-HA grown on the superhydrophilic VACNT, the

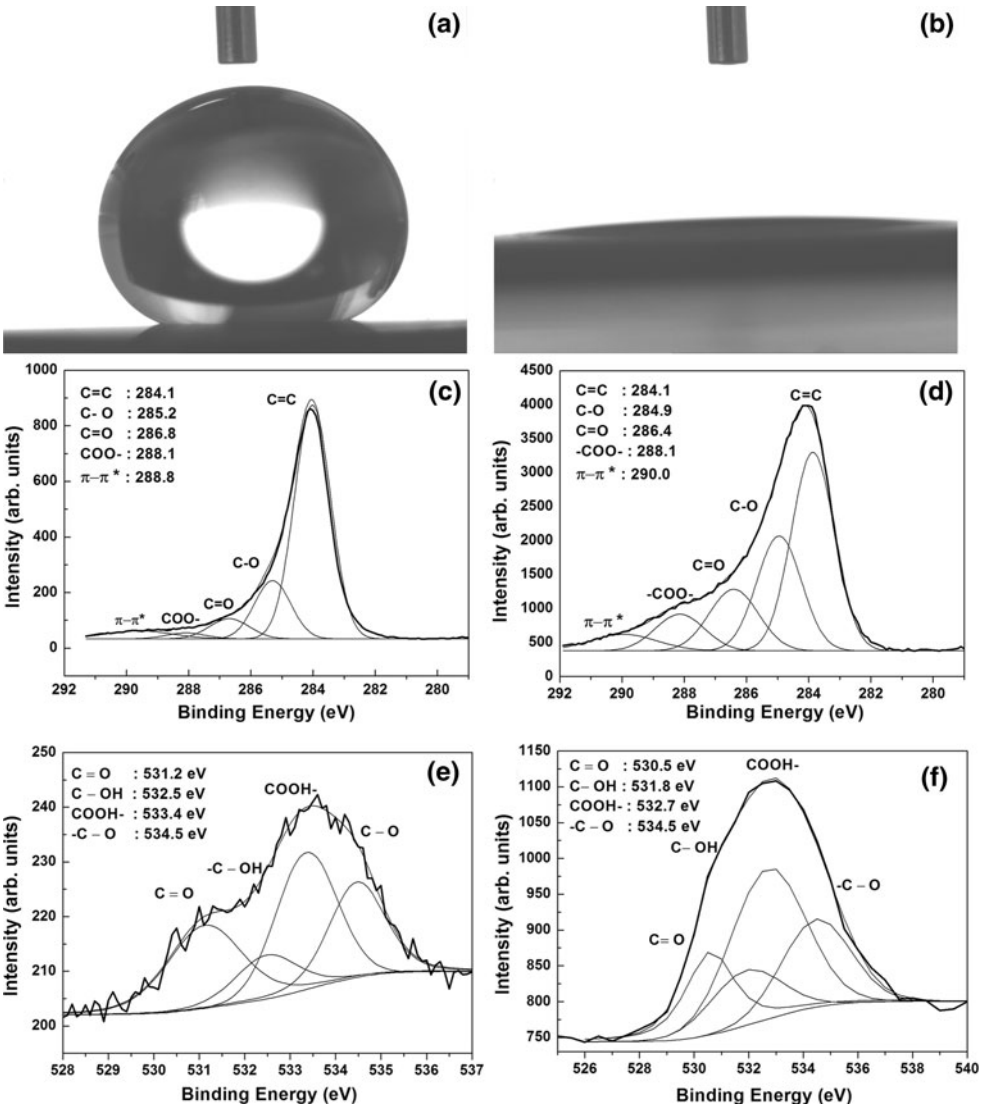

Fig. 2 Effect of oxygen plasma functionalization on the VACNTs. Optical microscopy images of the contact angle between deionized water and VACNT before (**a**) and after (**b**) the oxygen plasma treatment (magnification ×200). C1s XPS peak analysis before (**c**) and after (**d**) the oxygen plasma treatment. O1s XPS peak analysis before (**e**) and after (**f**) the oxygen plasma treatment

Table 1 Parameters collected from deconvolution of the C1s XPS peaks of VACNT films before and after oxygen plasma treatment

Peak	Position as grown (eV)	Intensity as-grown (arb. units)	FWHM as grown	Fitted area	Position hydrophilic (eV)	Intensity hydrophilic (arb. units)	FWHM hydrophilic	Fitted area
C=C	~284.1	~86,877.3	1.4	73,141.8	~284.1	~56,982.3	1.8	136,213.9
–C–O	~285.2	~84,455.5	1.3	12,492.7	~284.9	~53,455.5	1.8	16,966.6
–C=O	~286.8	~98,202.1	1.6	88,660.9	~286.4	~58,202.1	1.7	8,866.9
–COO	~288.1	~91,531.6	2.2	45,860.2	~288.1	~59,531.6	2.6	4,586.2
π–π*	~288.8	~86,877.3	3.1	45,860.2	~290.0	~51,877.3	3.4	4,586.2

higher crystallinity is evident with the small band FWHM of 12.5 cm^{-1}. Bands of lower intensities were observed at ~420, 580 and 780 cm^{-1} and attributed to other forms of apatites such as octacalcium phosphate and dicalcium phosphate dihydrates. The 1,030 cm^{-1} peak has been assigned to apatitic phosphate groups and is observed only in well-crystallized stoichiometric n-HA. The Raman band recorded at 1,040–1,045 cm^{-1} from an ex vivo human bone is assigned to P–O stretching [43]. Figure 5a also shows the VACNT Raman bands (D and G) [26, 27].

Figure 5b shows the FT-IR ATR analysis. The multiplets located around 1,000 cm^{-1} are attributed to phosphate modes. The split bands, mainly at 1,030 and 1,090 cm^{-1}, seem to correlate with the formation of a well-crystallized apatite. A more detailed analysis permits one to deduce the presence of a carbonated component, where carbonate ions

Table 2 Parameters collected from deconvolution of the O1s XPS peaks of VACNT films before and after oxygen plasma treatment

Peak	Position as grown (eV)	Intensity as grown (arb. units)	FWHM as grown	Fitted area	Position hydrophilic (eV)	Intensity hydrophilic (arb. units)	FWHM hydrophilic	Fitted area
C=O	~531.2	~21,841.7	~1.9	~3,517.5	~530.5	~37,745.2	~2.0	~73,226.5
C–OH	~532.5	~21,300.9	~1.6	~4,220.6	~531.8	~36,568.5	~2.6	~38,405.6
COOH–	~533.4	~23,177.2	1.4	~3,026.6	~532.7	~36,789.2	~2.7	~24,983.7
–C–O	~534.5	~22,640.1	1.6	~1,531.7	~534.5	~365,792.6	~2.3	~33,323.1

are substituting in A and B sites of the apatitic structure [45] (corresponding to phosphate and hydroxyl ions, respectively). Carbonate bands have been detected at 879, 1,415 and 1,455 cm^{-1}. Molecular and adsorbed water bands are also seen at 1,640 cm^{-1} (Fig. 5b).

Nucleation, in general, represents an activation energy barrier to the spontaneous formation of a solid phase from a supersaturated solution. This kinetic constraint may be sufficient to offset the thermodynamic driving force for precipitation, resulting in metastable solutions, which do not undergo phase transformations over a long period of time. The activation energy for nucleation (ΔG_N) is related to γ and ΔG_B by the equation [46]:

$$\Delta G_N = \frac{16\pi\gamma^3}{3(\Delta G_B)_2} \quad (1)$$

and

$$\Delta G_B = \frac{kT \ln S}{\upsilon}, \quad (2)$$

where k is the Boltzmann constant, T is the nucleation temperature, S is the relative supersaturation of the solution, γ is the solid/liquid interfacial energy, υ is the molecular volume and ΔG_B is the energy released in the formation of bonds in the bulk of the aggregate. The –COOH groups formed on superhydrophilic VACNT films after the oxygen plasma treatment (Fig. 2c–f) constructed ordered "recognized sites" with high polarity and charged density, which could draw the direct electrodeposition of the n-HA on them.

Liao et al. [47] suggested that dispersed CNTs provide abundant sites for nucleation of HA soaked in phosphate solution. They showed that the bamboo-like structure can be attributed to nucleation sites for HA formation. The electrodeposition of n-HA shown in Fig. 3a indicates that the growth only occurs on the top surface of the superhydrophilic VACNT. This top surface is heavily attacked by oxygen plasma, which is responsible for the grafting of the oxygen groups onto CNTs and a further roughening of the VACNT surfaces. Clearly, the rapid and direct electrodeposition of plate-like n-HA crystals on superhydrophilic VACNT films is highly influenced by the COOH groups identified by XPS. The enlargement of the COO^- band (288.1 eV) is due to a higher concentration of oxygen after the oxygen plasma treatment (around 18.93%). Both characteristics seem to be important to promote n-HA growth: some authors have already shown better HA growth on rough surfaces [1–4] and the mechanism of HA deposition depends on the liberation of OH^- ions, which may be enhanced by the presence of oxygen groups on surfaces [20–25, 48].

Other effects can also be directly affected by the HA electrodeposition [49, 50]. Ban and Maruno [49] demonstrated that the precipitation of calcium phosphate on the cathode is induced by the supersaturation of calcium phosphate salts due to the increase in pH and accumulation of both calcium and phosphate ions. The authors suggested that the needles grew up on the nuclei and the number of the nuclei decreased with the electrolyte temperature. These results imply that the hydrothermal–electrochemical deposition consists of two processes: nucleation and crystal growth. In this paper, we have shown that this property was essential for direct growth of n-HA on superhydrophilic VACNT.

In a previous work, a comparison between n-HA electrodeposition on NiTi alloys and on superhydrophilic VACNT films was reported. We showed that a direct plate-like n-HA crystal electrodeposition was only obtained on the superhydrophilic VACNT films, without any thermal and superficial treatment [26]. This can be interpreted with respect to supersaturation (due to a higher current density and electrical field) and crystal growth on $–COO^-$ groups attached to the superhydrophilic VACNT films.

Ban and Hasegawa [50] showed that surface reaction for HA crystal growth depends on whether the crystal faces are rough or smooth at the atomic level. The crystal tip formed at 100 °C showed smooth, flat and sharp-edged apatite, possibly formed due to the lateral growth mode at this temperature (plate-like HA crystals). After the bath temperature was adjusted to 200 °C, apatite grew by both adhesive and lateral growth modes, because the tips and edges were round, and some planes were smooth and flat (needle-like HA crystals). These authors concluded that both the precipitation and the crystal growth morphology of apatite strongly depend on the electrolyte temperature and slightly on the current density [49, 50]. In the present

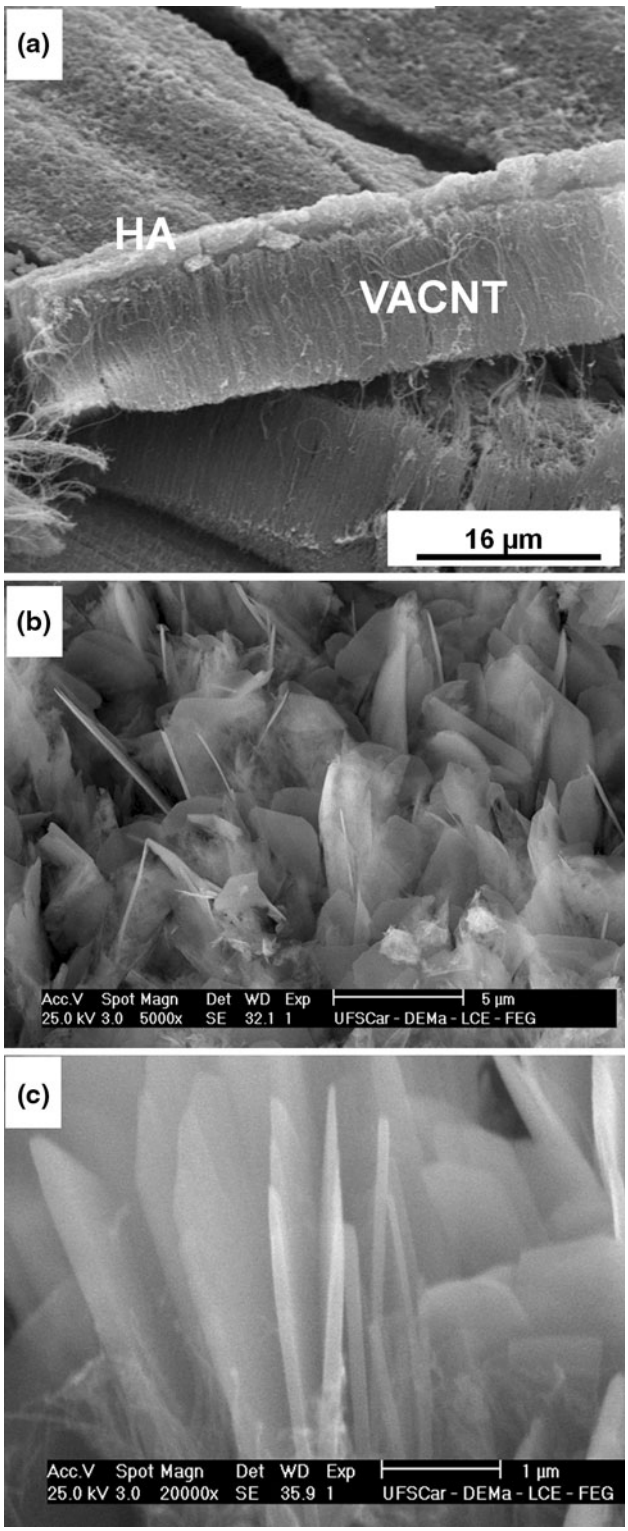

Fig. 3 **a** SEM image of the cross-section of plate-like n-HA film on top of the superhydrophilic VACNT films, **b–c** SEM images of direct electrodeposition of n-HA on VACNT films with increasing magnification

manuscript, in addition to investigating dependence on these two factors (electrolyte temperature and current density), we have shown that the plate-like n-HA crystal growth on superhydrophilic VACNT films is highly influenced by the nanotopology and wettability properties. The reason for this affirmation is a simple comparison between the same electrodeposition process applied using NiTi alloys [51] and superhydrophilic VACNT films [26] (temperature and current density). In this comparison, the n-HA crystal growth is only possible on NiTi alloys after roughening of the surface and thermal treatment. After roughening treatment, the NiTi alloys showed a circular morphology, which resulted in n-HA crystals with needle-like morphology. These crystals are different from plate-like n-HA crystals that are obtained on superhydrophilic VACNT films presented here. After these considerations were all taken into account, the proposed model of plate-like n-HA growth presented here is highly influenced by the nanotopology, current density and considerably by the carboxyl (carboxylic acid) groups directly attached to the superhydrophilic VACNT films before the oxygen plasma treatment.

The mechanism for n-HA crystal formation on superhydrophilic VACNT films is now proposed and discussed. The reaction of $(NH_4)H_2PO_4$ and $Ca(NO_3)_2$ produces NH_4NO_3 by Eq. 1, a very soluble compound [52] whose ions do not participate in the n-HA deposition reaction. The main reaction to produce n-HA is shown in reaction (3). The formation of $H_2PO_4^-$, HPO_4^{2-} and PO_4^{3-} has been explained in detail by Eliaz et al. [25].

$$2(NH_4)H_2PO_4 + Ca(NO_3)_2 \rightarrow 2NH_4NO_3 + Ca^{2+} + 2H_2PO_4^- \quad (3)$$

$$2H_2O + 2e^- \rightarrow H_2 + 2OH^- \quad (4)$$

$$10Ca^{2+} + 6H_2PO_4^- + 14OH^- \rightarrow Ca_{10}(PO_4)_6(OH)_2 + 12H_2O \quad (5)$$

Manso et al. showed that the deposition obtained with and without electrical activation demonstrates that the crystallization process at the interface is favored by electrical activation [24]. This means that cations are carried to the interface by OH^- anions while diffusing through the electrolyte. It is satisfactory to obtain a more homogeneous coating with activation, as it confirms that the drop of electric field on the deposited areas promotes deposition on the defect regions [24]. In this case, the superhydrophilic VACNT tips can be considered as active sites for crystal growth.

Three hypotheses about the HA electrodeposition process were proposed by other authors [25, 53–55]. The first one is that no charge evolution has been reported for HA particles in basic media [54], which excludes electrostatic forces as being responsible for a hypothetical indirect deposition. The second one is attributed to adherence of the coatings obtained at low voltages and high temperature, which is related to the diffusion of Ca^{2+} and specially P

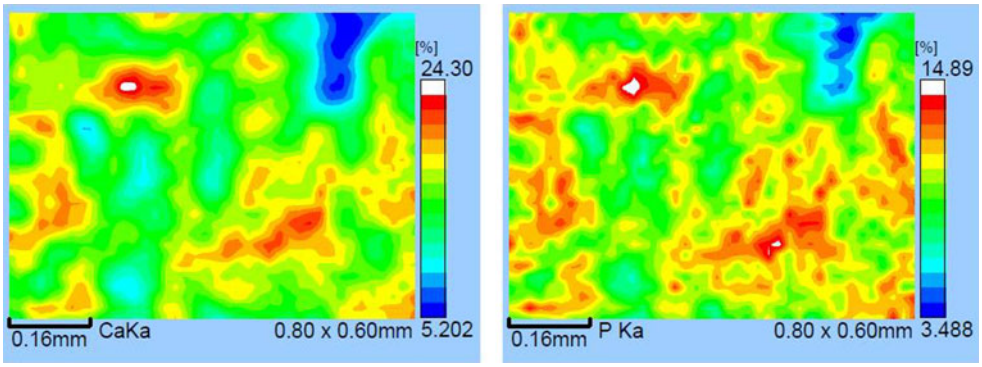

Fig. 4 Energy-dispersive X-ray mapping of plate-like n-HA electrodeposited on superhydrophilic VACNT films

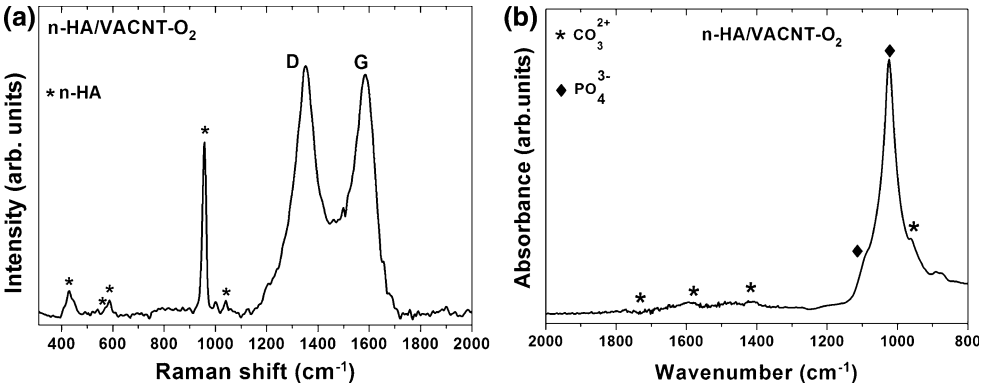

Fig. 5 Structural analysis of plate-like n-HA electrodeposited on superhydrophilic VACNT films. **a** Raman and **b** infrared spectra of n-HA obtained on the superhydrophilic VACNT films

species through the Ti substrate [48]. HA coatings obtained by indirect deposition at higher voltages with sequential sintering temperatures also produced HA films with good adhesion properties. The third one states that the low voltages applied in our experiment lead to current densities comparable to those used by other authors in acidic electrolytes. However, longer times for indirect deposition have been reported [25].

Our work presented a fast method to obtain plate-like n-HA crystals. The growth procedure for the formation of n-HA crystals essentially differs from the methods used by other authors. The OH^- discharging on the substrate from the water electrolysis in an acid medium is generally proposed, but after a longer time and thermal treatment. From this, the pH increases at the interface unchange the nucleation and promotes direct deposition [48–50]. The n-HA deposition on CNTs is only possible due to the –COOH terminations induced caused by the oxygen plasma etching. In this case, the electrostatic attraction of OH^- triggers the precipitation of HA nuclei at the interface and also leads to direct deposition. It was suggested that the formation of n-HA on the superhydrophilic VACNT tips was controlled by the charged density of chemical groups attached after the plasma treatment (Fig. 2c–f) and the interaction forces between the corresponding ionic groups and/or polar groups. Previous investigations of the nucleation sites of HA crystals on functionalized collagen fibers have suggested that the binding of calcium ions on the negatively charged carboxylate groups of collagen is one of the key factors for the first step of nucleation of HA crystals [56].

During the electrodeposition process, the carboxyl (carboxylic acid) groups may lose their hydrogen atoms and obtain negative electrical charges. The negative charge is evenly distributed on the two oxygen atoms. This negative charge is prone to attract positively charged calcium ions. Then, by exposing this reactive assemblage to phosphate and hydroxide ions, it is expected to form calcium phosphate on the superhydrophilic VACNT surface through the carboxyl functionalized site (after plasma treatment). This mechanism is believed to be responsible for the initiation of n-HA precipitation on the superhydrophilic VACNT surface [20, 57].

Figure 6 illustrates the establishment of ionic bonding between carboxylate groups and calcium ions, which are being electrodeposited into the HA solid structure during electrodeposition of plate-like n-HA crystals on VACNT films. The atomic Ca/P ratio of calcium phosphates directly electrodeposited on superhydrophilic VACNT films was $\sim$1.64 from the EDS analysis (data obtained after the quantitative analysis of Fig. 4), slightly lower than that of stoichiometric HA (1.67). It has been suggested that the carboxylate groups facilitate the initial electrodeposition of calcium ions, and the attraction of calcium ions is an important initial step in calcium phosphate formation [58]. The size of HA crystals is related to the available

nucleating sites [59–61]. With the increasing density of carboxylate groups, the abundant supply of coordination sites available for complexation with calcium ions led to a very large number of nuclei for the electrodeposition of n-HA crystalline material, resulting in smaller crystal size. The large amount of nuclei facilitates the homogeneous nucleation during electrodeposition, leading to precipitation and formation of apatite on the superhydrophilic VACNT films, as noted by the lower FWHM peak (data shown in Figs. 5a and 7). With this sequence of reactions, it is possible to revise the Saffar et al. [62] mechanism and a revised one can be proposed as presented in Fig. 6.

Cui et al. [63] proved that electrostatic attraction could be further facilitated by strong carboxylate interactions: $–COO^{-}Ca^{2+}$ or $(–COO^{-})_2Ca^{2+}$ interactions and the weaker hydroxyl interaction: $–OHCa^{2+}$, during the induction periods for apatite nucleation on polymer nanofibers using SBF solutions. After this, the positive charge of amino groups could form ionic bonds with carboxylate groups, which could accelerate phosphate ions on the RCa^{+}

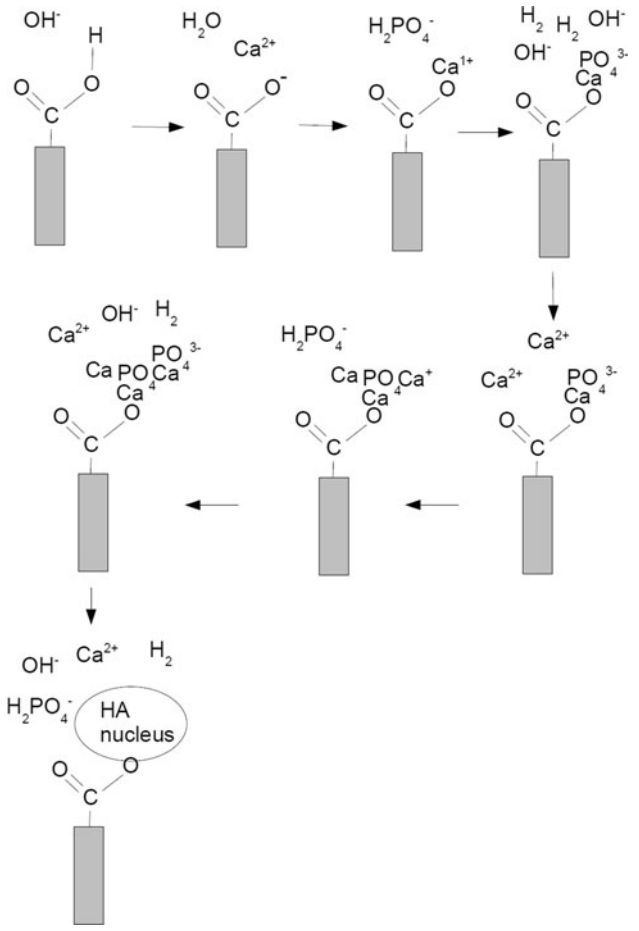

Fig. 6 Schematic illustration of plate-like n-HA crystals formation and dissolution during direct electrodeposition on superhydrophilic VACNTs surfaces based on Saffar et al. model [61]

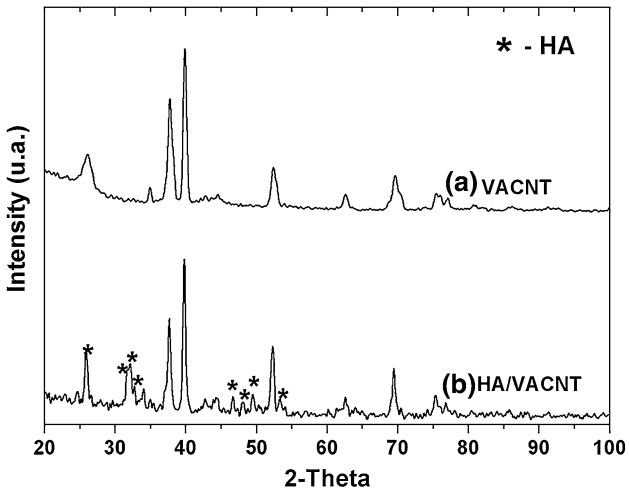

Fig. 7 X-ray diffractograms of as-grown VACNT (**a**) and plate-like n-HA crystals on superhydrophilic VACNT films (**b**)

to form HA. The proposed model presented here is the same, due to the higher network of carboxyl or carboxylate groups attached on superhydrophilic VACNT tips.

Saffar et al. [62] proposed a model of carboxylate/carboxyl (carboxylic acid) functionalized CNTs (CNT–COOH) to chemically synthesize HA, as an effective template. The authors showed that the calcium phosphate-like material induces ionic interaction with the ACOO's head group as a result of oppositely charged ions at the contact sites.

Figure 7 shows the X-ray diffraction pattern of the HA grown on superhydrophilic VACNT films. The diffraction peaks of the substrate are also shown for comparison. Notice that the apatite formation is deduced from the presence of several characteristic X-ray reflection peaks in the diffraction pattern shown. The principal diffraction peaks of HA appears at 2θ values of 25.9° for reflection (002), at 31.9° (triplet) for reflections (211), (112) and (300) and at 34.0° for reflection (200) (JCPDS 9-432) [26].

The broadening of a diffraction peak can be related to the mean crystallite size via the Scherer equation ($t = 0.89\lambda/B\cos\theta_B$) [48], where t is the mean crystallite size, B is the peak line-width at half maximum (in radian), θ_B is the Bragg diffraction angle and λ is the X-ray wavelength (CuKα radiation in our case).

A preference calculated from the XRD data was further explored as a structure indicator [32]. The relative intensity of the (002) peak (RI) to the intensities of the three strongest peaks for standard powder HA sample (JCPDS 9-432) is defined as:

$$\mathrm{RI} = \frac{I_{(002)}}{I_{(211)} + I_{(112)} + I_{(300)}}$$

where $I_{(002)}$, $I_{(211)}$, $I_{(112)}$ and $I_{(300)}$ are the XRD peak intensities of (002), (211),(112) and (300) planes,

Table 3 Parameters collected from deconvolution of the X-ray diffractogram of plate-like n-HA crystals electrodeposited on superhydrophilic VACNT films

Plane	Position (2-theta)	Intensity (arb. units)	Intensity (JPCD)[a]	FWHM	Crystallites (nm)	Preference growth, P
(002)	25.9	0.45	0.4	0.46	2.9	1.5
(211)	31.7	0.32	1.0	0.31	4.4	−0.5
(112)	32.2	0.34	0.6	0.50	2.7	0.1
(300)	32.7	0.23	0.6	0.24	5.7	−0.2

All the crystallite sizes and growth preferences determined for the planes are shown. The JPCDS 9-432 was used for comparison

[a] Data collected for HA standard powder (JPCD 9-432) for preference growth compute

respectively. For the standard powder, HA calculated using JCPDS 9-432, $RI_s = 0.1818$ for the (002) peak. A similar value was obtained by Hu et al. [32]. Each peak has its own Ri and RI_s. In this work, the preference, P, is defined as the relative difference of RI from RI_s:

$$P = \frac{RI - RI_s}{RI_s}$$

Table 3 shows all the data used to calculate the crystallite size and growth preference. These data were collected from three different points and samples. The mean was expressed for comparison.

HA has a hexagonal space group of p63/m with $a = 0.9430$ nm and $c = 0.6891$ nm. The O–H groups are ordered on the c-axis or in the (002) plane. For HA with a hexagonal structure, the [001] direction is the usual direction for preferred growth, along which the crystal planes are most densely populated with atoms. Calculations identified preferential growth along the (002) plane, and secondly, along the (112) plane. The negative value was attributed to suppression of the (211) and (300) planes due to higher growth preference for the (002) plane (data shown in Table 3). In the case of superhydrophilic VACNT, the thickness of the plate-like structure is very close to the crystallite size obtained using Scherer formula from the X-ray diffractogram (Table 3). This indicates that each platelet is a single plate-like n-HA crystal. So, the (002) crystalline planes whose axes are along in the [001] direction would grow preferentially [24–26, 64]. The higher intensity of the (002) plane shows a standard n-HA growth pattern on superhydrophilic VACNT. The high frequency of these planes may be related to a plate-like morphology, as evident in Fig. 2b and c. Probably, the expression of previous plate-like morphology of n-HA indicates some selectivity in surface binding. Filgueiras et al. [65], using computational modeling, attributed the plate-like morphology of HA in terms of the surface energy. In the view of surface energy, the surface energy of (100) planes is higher than (001) planes [65]. In other words, the (100) planes are relatively less stable. The less-stable terminations will be more reactive and may quickly accumulate more HA material including inhibiting adsorbates to form more stable terminations [65]. Besides, the (100) planes contain loci of positive charges centered on calcium ions [65].

A similar phenomenon of preferred orientation of apatite coatings on titanium substrates has been reported earlier [24, 25, 64], but they were obtained only after thermal annealing around at 900 °C. Further studies should be carried out using different electrolytes, pH and temperatures to obtain thermodynamic considerations about plate-like n-HA crystal growth directly electrodeposited on superhydrophilic VACNT films.

4 Conclusions

In this work, we have presented a mechanism for the preferential growth of n-HA plate-like crystals directly electrodeposited on superhydrophilic VACNT films. The plate-like HA crystal formation is due to the –COOH terminations that were attached to VACNT tips after oxygen plasma etching. A preferential growth of plate-like n-HA crystals in the (002) plane was observed.

Acknowledgments This work was supported by FAPESP (07/00013-4, 06/03525-3). Special thanks to Maria Lucia Brison (LAS/INPE) for the SEM images, Diego Davi Coimbrão (UFSCar) for the high-resolution SEM and Marcelo E. H. Maia da Costa (PUC/Rio) for the XPS spectra. We would also like to thank the referees for the comments and recommendations on how to improve our work. We also very grateful for the special attention given by Professor Karl J. Jalkanen to improved the quality of this manuscript.

References

1. LeGeros RZ (2002) Properties of osteoconductive biomaterials: calcium phosphates. Clin Orthop Relat Res 395:81–98
2. Oyane A, Onuma K, Ito A, Kim HM, Kokubo T, Nakamura T (2003) Formation and growth of clusters in conventional and new kinds of simulated body fluids. J Biomed Mater Res A 64A:339–348

3. Vallet-Regi M, Gonzalez-Calbet JM (2004) Calcium phosphates as substitution of bone tissues. Prog Solid State Chem 32:1–31
4. Berman A, Ahn DJ, Lio A, Salmeron M, Reichert A, Charych D (1995) Total alignment of calcite at acidic polydiacetylene films: cooperativity at the organic-inorganic interface. Science 269:515–518
5. Balasundaram G, Webster TJ (2006) Nanotechnology and biomaterials for orthopedic medical applications. Nanomedicine 1:169–176
6. Correa-Duarte MA, Wagner N, Rojas-Chapana J, Morsczeck C, Thie M, Giersig M (2004) Fabrication and biocompatibility of carbon nanotube-based 3D networks as scaffolds for cell seeding and growth. Nanoletters 4:2233–2236
7. Lobo AO, Corat MAF, Antunes EF, Palma MBS, Pacheco-Soares C, Garcia EE, Corat EJ (2010) An evaluation of cell proliferation and adhesion on vertically-aligned multi-walled carbon nanotube films. Carbon 48:245–254
8. Nguyen-Vu TDB, Hua C, Cassell AM, Andrews RJ, Meyyappan M, Jun L (2007) Vertically aligned carbon nanofiber architecture as a multifunctional 3-D neural electrical interface. IEEE Trans Biomed Eng 54:1121–1128
9. Cai N, Wong CC, Gong YX, Tan SCW, Chan V, Liao K (2010) Modulating cell adhesion dynamics on carbon nanotube monolayer engineered with extracellular matrix proteins. ACS Appl Mater Interfaces 2:1038–1047
10. Namgung S, Kim T, Baik KY, Lee M, Nam JM, Hong S (2011) Fibronectin-carbon-nanotube hybrid nanostructures for controlled cell growth. Small 7:56–61
11. Salvetat JP, Bonard JM, Thomson NH, Kulik AJ, Forro L, Benoit W, Zuppiroli L (1999) Mechanical properties of carbon nanotubes. Appl Physa A-Mater 699:255–260
12. Endo M, Strano MS, Ajayan PM (2008) Potential applications of carbon nanotubes. Top Appl Phys 111:13–61
13. Bhattacharyya S, Guillott S, Dabboue H, Tranchant JF, Salvetat JP (2008) Carbon nanotubes as structural nanofibers for hyaluronic acid hydrogel scaffolds. Biomacromolecules 9:505–509
14. Cui D (2007) Advance and prospects of biomolecules functionalized carbon nanotubes. J Nanosci Nanotech 7:1298–1314
15. Ishizaki T, Saito N, Osamu Takai O (2010) Correlation of cell adhesive behaviors on superhydrophobic, superhydrophilic, and micropatterned superhydrophobic/superhydrophilic surfaces to their surface chemistry. Langmuir 26:8147–8154
16. Kim Y, Lee D, Oh Y, Choi J, Baik S (2006) The effects of acid treatment methods on the diameter dependent length separation of single walled carbon nanotubes. Synth Met 156:999–1003
17. Lakshminarayanan PV, Toghiani H Jr, Pittman CU (2004) Nitric acid oxidation of vapor grown carbon nanofibers. Carbon 42:2433–2442
18. Liu M, Yang Y, Zhu T, Liu Z (2005) Chemical modification of single-walled carbon nanotubes with peroxytrifluoroacetic acid. Carbon 43:1470–1478
19. Ramos SC, Vasconcelos G, Antunes EF, Lobo AO, Trava-Airoldi VJ, Corat EJ (2010) CO_2 laser treatment for stabilization of the superhydrophobicity of carbon nanotube surfaces. J Vac Sci Technol B 28:1153–1158
20. Aryal S, Bahadur KCR, Dharmaraj N, Kim KW, Kim HY (2006) Synthesis and characterization of hydroxyapatite using carbon nanotubes as a nanomatrix. Scripta Mater 54:131–135
21. Boccaccinia AR, Choa J, Subhania T, Kayab C, Kayac F (2010) Electrophoretic deposition of carbon nanotube-ceramic nanocomposites. J Eur Ceram Soc 30:1115–1129
22. Hahna B-D, Lee J-M, Park D-S, Choi J–J, Ryua J, Yoon W-H, Lee B-K, Shin D-S, Kim H-E (2009) Mechanical and in vitro biological performances of hydroxyapatite–carbon nanotube composite coatings deposited on Ti by aerosol deposition. Acta Biomater 5:3205–3214
23. Najafi H, Nemati ZA, Sadeguian Z (2009) Inclusion of carbon nanotubes in a hydroxyapatite sol–gel matrix. Cer Inter 35:2987–2991
24. Manso M, Jiménez C, Morant C, Herrero P, Martínez-Duart JM (2000) Electrodeposition of hydroxyapatite coatings in basic conditions. Biomaterials 21:1755–1761
25. Eliaz N, Eliyahu M (2007) Electrochemical processes of nucleation and growth of hydroxyapatite on titanium supported by realtime electrochemical atomic force microscopy. J Biomed Mater Res A 80:621–634
26. Lobo AO, Corat MAF, Ramos SC, Matsushima JT, Granato AEC (2010) Fast preparation of hydroxyapatite/superhydrophilic vertically aligned multiwalled carbon nanotube composites for bioactive application. Langmuir 26(23):18308–18314
27. Antunes EF, Lobo AO, Corat EJ, Trava-Airoldi VJ, Martin AA, Veríssimo C (2006) Comparative study of first- and second-order Raman spectra of MWCNT at visible and infrared laser excitation. Carbon 44:2202–2221
28. Antunes EF, Lobo AO, Corat EJ, Trava-Airoldi VJ (2007) Influence of diameter in the Raman spectra of aligned multiwalled carbon nanotubes. Carbon 45:913–921
29. Lobo AO, Corat MAF, Antunes EF, Ramos SC, Pacheco-Soares C, Corat EJ (2010) Cytocompatibility studies of vertically-aligned multi-walled carbon nanotubes: raw material and functionalized by oxygen plasma. Mater Sci Eng C. doi: 10.1016/j.msec.2010.08.010
30. Marciano FR, Marcuzzo JS, Bonetti LF, Corat EJ, Trava-Airoldi VJ (2009) Use of near atmospheric pressure and low pressure techniques to modification DLC film surface. Surf Coat Tech 204:64–68
31. Ramos SC, Vasconcelos G, Antunes EF, Lobo AO, Trava-Airoldi VJ, Corat EJ (2010) Wettability control on vertically-aligned multi-walled carbon nanotube surfaces with oxygen pulsed DC plasma and CO_2 laser treatments. Diam Relat Mater 19:752–755
32. Hua R, Lin C, Shi H, Wanga H (2009) Electrochemical deposition mechanism of calcium phosphate coating in dilute Ca–P electrolyte system. Mater Chem Phys 115:718–723
33. Hueso JL, Espino JP, Caballero A, Cotrino J, Gonzalez-Elipe AR (2007) XPS investigation of the reaction of carbon with NO, O_2, N_2 and H_2O plasmas. Carbon 45:89–96
34. Datsyuk V, Kalyv M, Papagelis K, Parthenios J, Tasis D, Siokou A, Kallitsis I, Galiotisa C (2008) Chemical oxidation of multiwalled carbon nanotubes. Carbon 46:833–840
35. Lu Y, Li W, Sun F, Zhao L, Xing L (2010) Highly hydroxylated carbon fibres as electrode materials of all-vanadium redox flow battery. Carbon 48:3079–3090
36. Estrade-Szwarckopf H (2004) XPS photoemission in carbonaceous materials: a ''Defect'' peak beside the graphitic asymmetric peak. Carbon 42:1713–1721
37. Okpalugo TIT, Papakonstantinou P, Murphy H, McLaughlin J, Brown NMD (2005) High resolution XPS characterization of chemical functionalized MWCNTs and SWCNTs. Carbon 43:153–161
38. Gerin PA, Dengis PB, Rouxhet PG (1995) Performance of XPS analysis of model biochemical compounds. J Chim Phy 92:1043–1065
39. Elzbieta P, Paul R (2003) Bulk and surface chemical functionalities of type III PAN-based carbon fibres. Carbon 41:1905–1915
40. Moulder JF, Stickle WF, Sobol PE, Bomben KD (1995) Handbook of X-ray photoelectron spectroscopy, perkin-elmer corporation. Eden Prairie, MN
41. Xu T, Yang J, Liu J, Fu Q (2007) Surface modification of multiwalled carbon nanotubes by O_2 plasma. Appl Surf Sci 253:8945–8951
42. Chirila V, Marginean G, Brandl W (2005) Effect of the oxygen plasma treatment parameters on the carbon. Surf Coat Tech 200:548–551

43. Brandl W, Marginean G (2004) Functionalization of the carbon nanofibres by plasma treatment. Thin Solid Films 447:181–186
44. Kale S, Biermann S, Edwards C, Tarnowski C, Morris M, Long MW (2000) Three dimensional cellular development is essential for ex vivo formation of human bone. Nature Biotechnol 18:954–958
45. Elliot JC (1994) Structure and chemistry of the apatites and other calcium orthophosphates, chap 3. Elsevier, Amsterdam
46. Liu Y, Huang S, Dan X, Zhou K (2004) Growth of hydroxyapatite crystal in the presence of organic film. J Mater Sci Technol 20:223–226
47. Liao S, Xu G, Wang W, Watari F, Cui F, Ramakrishna S, Chan CK (2007) Self- assembly of nano-hydroxyapatite on multiwalled carbon nanotubes. Acta Biomater 3:669–675
48. Barrere F, Snel MME, Blitterswijka A, de Klaas G, Layrolle P (2004) Nanoscale study of the nucleation and growth of calcium phosphate coating on titanium implants. Biomaterials 25:2901–2910
49. Ban S, Maruno S (1993) Deposition of calcium phosphate on titanium by electrochemical process in simulated body fluid. Jpn J Appl Phys 32:L1577–L1580
50. Ban S, Hasegawa J (2002) Morphological regulation and crystal growth of hydrothermal electrochemically deposited apatite. Biomaterials 23:2965–2972
51. Lobo AO, Otubo J, Matsushima JT, Corat EJ (2011) Rapid obtaining of nano-hydroxyapatite bioactive films on NiTi shape memory alloy by electrodeposition process. J Mater Eng Perform 20:793–797
52. Patnaik P (2003) Handbook of inorganic chemicals. McGraw-Hill, NY, ISBN:0070494398
53. Pezzatini S, Solito R, Morbidelli L, Lamponi S, Boanini E, Bigi A, Ziche M (2006) The effect of hydroxyapatite nanocrystals on microvascular endothelial cell viability and functions. J Biomed Mater Res 76A:656–663
54. Damodaran R, Moudgil BM (1993) Electrophoretic deposition of calcium phosphates from non-aqueous media. Colloid Surf A Physicochem Eng Aspects 80:191–195
55. Redepenning J, Schlessinger T, Burnhum S, Lipiello L, Miyano J (1996) Characterization of electrolytically prepared brushite and hydroxyapatite coating on orthopaedic alloys. J Biomed Mater Res 30:287–294
56. Kikuchi M, Itoh S, Ichinose S, Shinomiya K, Tanaka J (2001) Self-organization mechanism in a bone-like hydroxyapatite/collagen nanocomposite synthesized in vitro and its biological reaction in vivo. Biomaterials 22:1705–1711
57. Aryal S, Bhattarai SR, Bahadur KCR, Khil MS, Lee D-R, Kim HY (2006) Carbon nanotubes assisted biomimetic synthesis of hydroxyapatite from simulated body fluid. Mater Sci Eng A 426:202–207
58. Kawashita M, Nakao M, Minoda M, Kim H, Beppu T, Miyamoto T et al (2003) Apatite forming ability of carboxyl group-containing polymer gels in a simulated body fluid. Biomaterials 24:2477–2484
59. Takeuchi A, Ohtsuki C, Miyazaki T, Tanaka H, Yamazaki M, Tanihara M (2003) Deposition of bone-like apatite on silk fiber in a solution that mimics extracellular fluid. J Biomed Mater Res 65:283–289
60. Toworfe G, Composto R, Shapiro I, Ducheyne P (2006) Nucleation and growth of calcium phosphate on amine-, carboxyl- and hydroxyl-silane self-assembled monolayers. Biomaterials 27:631–642
61. Mollazadeh S, Javadpour J, Khavandi A (2007) In situ synthesis and characterization of nano-size hydroxyapatite in poly(vinyl alcohol) matrix. Ceram Int 33:15791583
62. Saffar KP, Arshi AR, Jamilpour N, Najafi AR, Rouhi G, Sudak L (2010) A cross-linking model for estimating young′s modulus of artificial bone tissue grown on carbon nanotube scaffold. J Biomed Mater Res A 94:594–602
63. Cui W, Li X, Xie C, Zhuang H, Zhou S, Weng J (2010) Hydroxyapatite nucleation and growth mechanism on electrospun fibers functionalized with different chemical groups and their combinations. Biomaterials 31:4620–4629
64. Vijayaraghavan TV, Benesalem A (1994) Electrodeposition of apatite coating on pure titanium and titanium alloys. J Mater Sci Lett 13:1782–1785
65. Filgueiras MRT, Mkhonto D, de Leeuw NH (2006) Computer simulations of the adsorption of citric acid at previous term-hydroxyapatitenext term surfaces. J Cryst Growth 294:60–68